

Cavity-coupled telecom atomic source in silicon

Received: 29 November 2023

Accepted: 5 March 2024

Published online: 15 March 2024

Adam Johnston ^{1,2,4}, Ulises Felix-Rendon ^{1,2,4}, Yu-En Wong ^{1,2,4} & Songtao Chen ^{1,3} ✉

Novel T centers in silicon hold great promise for quantum networking applications due to their telecom band optical transitions and the long-lived ground state electronic spins. An open challenge for advancing the T center platform is to enhance its weak and slow zero phonon line (ZPL) emission. In this work, by integrating single T centers with a low-loss, small mode-volume silicon photonic crystal cavity, we demonstrate an enhancement of the fluorescence decay rate by a factor of $F = 6.89$. Efficient photon extraction enables the system to achieve an average ZPL photon outcoupling rate of 73.3 kHz under saturation, which is about two orders of magnitude larger than the previously reported value. The dynamics of the coupled system is well modeled by solving the Lindblad master equation. These results represent a significant step towards building efficient T center spin-photon interfaces for quantum information processing and networking applications.

Optically interfaced atomic defects in solid-state materials are important building blocks for a variety of quantum technologies¹. For example, nitrogen and silicon vacancy centers in diamonds have been used to demonstrate milestone results for fiber-based quantum networks, including spin-photon entanglement², deterministic entanglement generation between remote spins³, quantum state teleportation⁴, and memory-enhanced communication⁵. However, these defects have optical transitions at the visible or near-infrared spectral range resulting in large fiber transmission loss, requiring nonlinear frequency conversion⁶ to extend the network range. Significant progress has been made towards utilizing atomic defects with telecom optical transitions, leading to the discovery of single vanadium ions in silicon carbide⁷, defects in gallium nitride⁸, and single erbium ions in yttrium orthosilicate⁹, as well as a recent demonstration of indistinguishable telecom photon generation from single erbium ions¹⁰.

Early exploration into the scalable fabrication of atomic defects with photonic structures relies on heterogeneous material integration and typically involves pick-and-place type of fabrication procedures^{9,11,12}. On the other hand, silicon-on-insulator (SOI) is a mature and scalable platform to enable large-scale monolithic

photonic and electronic device integration. Telecom-interfaced solid-state spins in silicon can thus benefit from the technological advantages of the SOI platform, and be utilized for realizing large-scale spin-based integrated quantum photonic chips¹³. Moreover, silicon can be isotopically enriched to create a “semiconductor vacuum”¹⁴ for lowering the magnetic noise generated from the ²⁹Si nuclear spin bath.

Beyond efforts towards optical addressing of erbium ions in silicon^{15–17}, multiple novel atomic defect centers in silicon, including C, G, T, and W centers^{18–27}, have been experimentally identified recently towards quantum information applications. Among them, T centers are particularly promising due to their telecom O-band optical transitions, doublet ground state spin manifold, and long spin coherence times in an enriched ²⁸Si sample²³. Single T centers have been isolated in micropuck²⁴ and waveguide²⁸ structures. To further advance the single T center platform for quantum networking applications, challenges remain to enhance its weak and slow coherent emission at the zero phonon line (ZPL). The cavity-induced Purcell effect²⁹ has been widely used for enhancing the fluorescence emission of various atomic defects in solids, including G centers^{30–32}.

In this work, we demonstrate Purcell enhancement of a single T center in a low-loss, small mode-volume silicon photonic crystal (PC)

¹Department of Electrical and Computer Engineering, Rice University, Houston, TX 77005, USA. ²Applied Physics Graduate Program, Smalley-Curl Institute, Rice University, Houston, TX 77005, USA. ³Smalley-Curl Institute, Rice University, Houston, TX 77005, USA. ⁴These authors contributed equally: Adam Johnston, Ulises Felix-Rendon, Yu-En Wong. ✉ e-mail: songtao.chen@rice.edu

cavity. When the cavity is tuned into resonance with the single T center we observe an enhancement of its fluorescence decay rate by a factor of $F=6.89$, shortening the single T center lifetime to 136.4 ± 0.6 ns. Leveraging the nanophotonic circuit and an angle-polished fiber for light coupling³³, the system detection efficiency reaches $\eta_{\text{sys}} = 9.1\%$, representing the probability of a single photon emitted into the cavity being registered by the detector. This efficiency is 20-fold larger than that achieved in a typical confocal-type measurement system for T centers. We probe single T centers in the device using time-resolved photoluminescence excitation (PLE) spectroscopy. Under the pulsed excitation, the system can detect 0.01 ZPL photon per excitation, reaching an average photon count rate of 73.3 kHz, which is about two orders of magnitude improvement from the previously reported emission rate for single T centers in the waveguide²⁸. By solving the Lindblad master equation, we develop a numerical model to describe the coupling dynamics between the single T center and the cavity, and extract cavity-QED parameters as well as T center pure dephasing rate (Γ_d) and spectral diffusion (Γ_{sd}). This work represents a key step towards utilizing single T centers in silicon for quantum information applications.

Results

Device integration and PLE spectroscopy

Our experimental configuration is outlined in Fig. 1a. The nanophotonic devices are fabricated on a SOI sample which is situated on the cold finger of a closed-cycle cryostat ($T = 3.4$ K). Each device consists of a subwavelength grating coupler (GC)³⁴ and a one-dimensional PC cavity, which is connected by a linearly tapered waveguide (Fig. 1b). Optical coupling to the PC cavities is accomplished by using an angle-polished fiber via the GC with a one-way coupling efficiency of $\eta_{\text{GC}} = 46.1\%$ at 1326 nm (Fig. 1c). The fiber is mounted on a three-axis translation stage for optimizing the coupling. The PC cavity used in this work (Fig. 1d) has a quality factor $Q = 4.3 \times 10^4$. Fluorescence from the T center is detected by a fiber-coupled superconducting nanowire single photon detector (SNSPD) located in a separate cryostat (Fig. 2a). To match the atomic transition, we coarsely red-tune the cavity resonance by condensing nitrogen gas onto the surface of the device; we fine blue-tune the cavity resonance by sending laser pulses with a high optical power into the cavity (Supplementary Section 1.2).

T centers are generated in the middle of the device layer (220 nm in thickness) of the SOI samples using the ion implantation method³⁵.

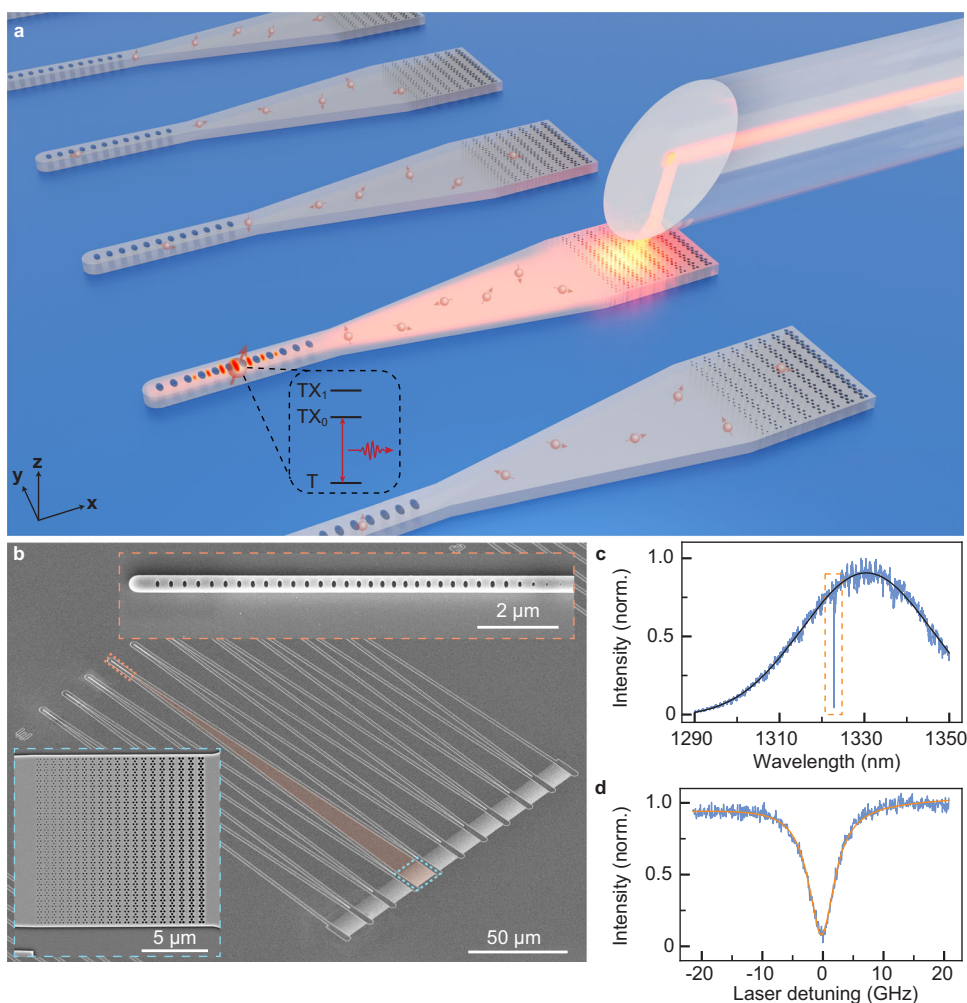


Fig. 1 | Efficient optical coupling to single T centers in a silicon photonic cavity. **a** Schematic illustration of fiber coupling to the nanophotonic circuits. Each PC cavity and subwavelength GC (with a width of 13.1 μm) are connected via a linearly tapered waveguide (200 μm in length). The GC allows efficient light coupling with an angle-polished fiber. (x, y, z) refer to $([0\bar{1}0], [100], [001])$ directions of the silicon crystal. T centers (solid red balls with arrows) are uniformly generated across the whole SOI device layer using the ion implantation method. Inside the dashed square, the simplified electronic level structure of the single T center is shown²³.

b Scanning electron microscope image of a block of 10 devices. An individual device (orange-shaded) consists of a PC cavity on the upper left end (inside the orange dashed rectangle) and a GC on the lower right end (inside the blue dashed rectangle). **c** Measured GC coupling spectrum (blue), with a Gaussian (black) fitted FWHM linewidth of 36.1 nm. The orange dashed box encloses a PC cavity. **d** Reflection spectrum of the cavity (blue) shown in panel (c), with a Lorentzian (orange) fitted FWHM linewidth of 5.22 ± 0.04 GHz. This cavity is used in later experiments. Results shown in panel (c) and (d) are measured at $T = 3.4$ K.

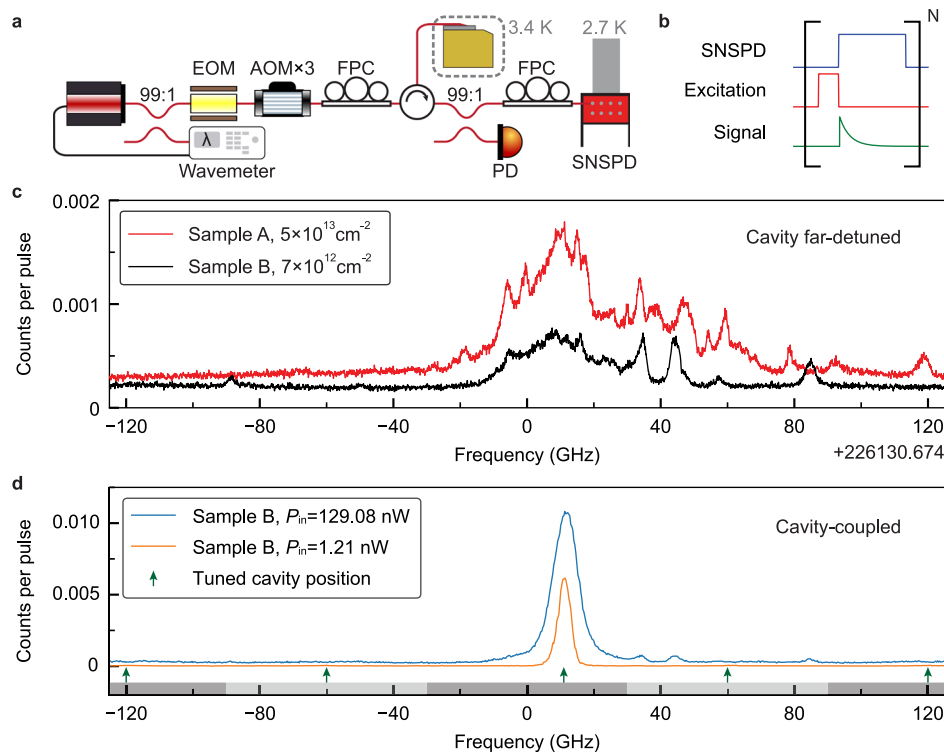


Fig. 2 | Photoluminescence excitation spectroscopy for T centers. **a** Simplified schematic of the experimental setup for performing PLE spectroscopy. Short excitation pulses are generated via a series of acousto-optic modulators (AOMs) and an electro-optic modulator (EOM) from a stabilized laser. The EOM is also used to generate laser sidebands. Fluorescence photons are redirected via an optical circulator to a SNSPD in another cryostat with $T = 2.7$ K for detection. A small portion of the signal enters a photodiode (PD) for monitoring cavity reflection. FPC: fiber polarization controller. **b** PLE pulse sequence. The SNSPD is gated to prevent detector latching due to the strong laser excitation pulses. **c** PLE spectrum for two different implanted SOI samples under similar excitation conditions when the

cavity is far-detuned ($\Delta_{ac} > 200$ GHz). The vertical axis indicates the average number of photons detected in a $5.55 \mu\text{s}$ integration window after each excitation pulse. Both samples are implanted with 1:1 ratio of ^{12}C and ^1H , and the implantation fluences are labeled in the legend. All the frequencies in this paper, if not specified, are offset from a reference $f_0 = 226130.674$ GHz (1325.749 nm or 935.201 meV). **d** PLE spectrum for sample B at different excitation powers when the cavity is tuned within the scanning range. Each tuned cavity position is indicated by a green arrow, with the corresponding laser scanning range shaded on the x-axis under the arrow. The spectrum shows a dominant peak, which we interpret as a single T center coupled to the cavity.

Each SOI sample is implanted sequentially with 1:1 ratio of $35 \text{ keV } ^{12}\text{C}$ and $8 \text{ keV } ^1\text{H}$ ions, with rapid thermal annealing performed in between and after the implantation steps (Supplementary Section 3.1). The two samples shown in this work have an implantation fluence of $5 \times 10^{13} \text{ cm}^{-2}$ (sample A) and $7 \times 10^{12} \text{ cm}^{-2}$ (sample B), respectively, which result in different T center densities after the generation process. To search for T centers, we perform time-resolved PLE spectroscopy by scanning the wavemeter-stabilized laser around the reported inhomogeneous center of T centers in silicon^{23,24,35}, with the pulse sequence shown in Fig. 2b.

First, we measure the spectrum with the cavity far-detuned from the scan range (Fig. 2c). The inhomogeneous distribution linewidth is about $\Gamma_{\text{inh}} \approx 29$ GHz. Isolated peaks can be observed away from the inhomogeneous center, which we interpret as the optical transitions of T centers that are likely located inside the taper waveguide. These peaks have an average full-width half maximum (FWHM) linewidth of 2.40 ± 0.86 GHz, and a fluorescence lifetime of 836.8 ± 57.3 ns (Supplementary Section 4), which is slightly shorter than the bulk T centers' lifetime of 940 ns²³. The estimated T center densities are $\sim 1 \times 10^{12} \text{ cm}^{-3}$ and $\sim 3 \times 10^{11} \text{ cm}^{-3}$ for sample A and B, respectively (Supplementary Section 3.1). To gauge the probability of an excited T center emitting a photon into the waveguide mode, we analyze a typical waveguide-coupled T center (at 46 GHz in sample B); we use the bounded T center quantum efficiency (discussed below) to estimate its emission efficiency to the waveguide mode as $2.6\% \leq \eta_{\text{wg}} \leq 10.9\%$ (Supplementary Section 4).

Next, we scan the laser frequency with the cavity tuned in-range to obtain the cavity-coupled PLE spectrum (Fig. 2d). In sample B, a new T center peak at the inhomogeneous center emerges with its fluorescence significantly surpassing all other peaks. This cavity-coupled T center has a FWHM linewidth of $\Gamma = 3.81 \pm 0.07$ GHz under a low excitation power (Fig. 3a). To verify the peak originates from a single T center, we measure the second-order autocorrelation function $g^{(2)}$ using all the detected fluorescence photons after each excitation pulse (Fig. 3b). Photon antibunching is observed with the value $g^{(2)}(0) = 0.024 \pm 0.018$, which confirms the majority of the detected photons come from a single emitter. This is the lowest $g^{(2)}(0)$ value ever observed for single T centers, and is comparable or better than other defect-based telecom emitters in solids^{7–10,20,27,36}. Autocorrelation measurements for the single T center can show bunching ($g^{(2)}(n) > 1$, when $|n| \geq 1$) under certain excitation conditions, which we speculate to be caused by spectral diffusion (Supplementary Section 5.3).

The emission amplitude of the cavity-coupled single T center saturates at 0.01 photons per excitation pulse (Fig. 3c). Both the saturation and power-dependent linewidth (Fig. 3d) are well described by the numerical modeling (discussed below). The measured $g^{(2)}(0)$ at higher powers (Fig. 3d) is limited by the accidental coincidences from background T centers' emission (Supplementary Section 5.2). To characterize the spectral diffusion, we monitor the spectrum of the cavity-coupled single T center over a few hours time span by taking repetitive PLE scans (Fig. 3e), which reveals a spectrum-center distribution of 11.30 ± 0.13 GHz. A similar level of spectral diffusion is

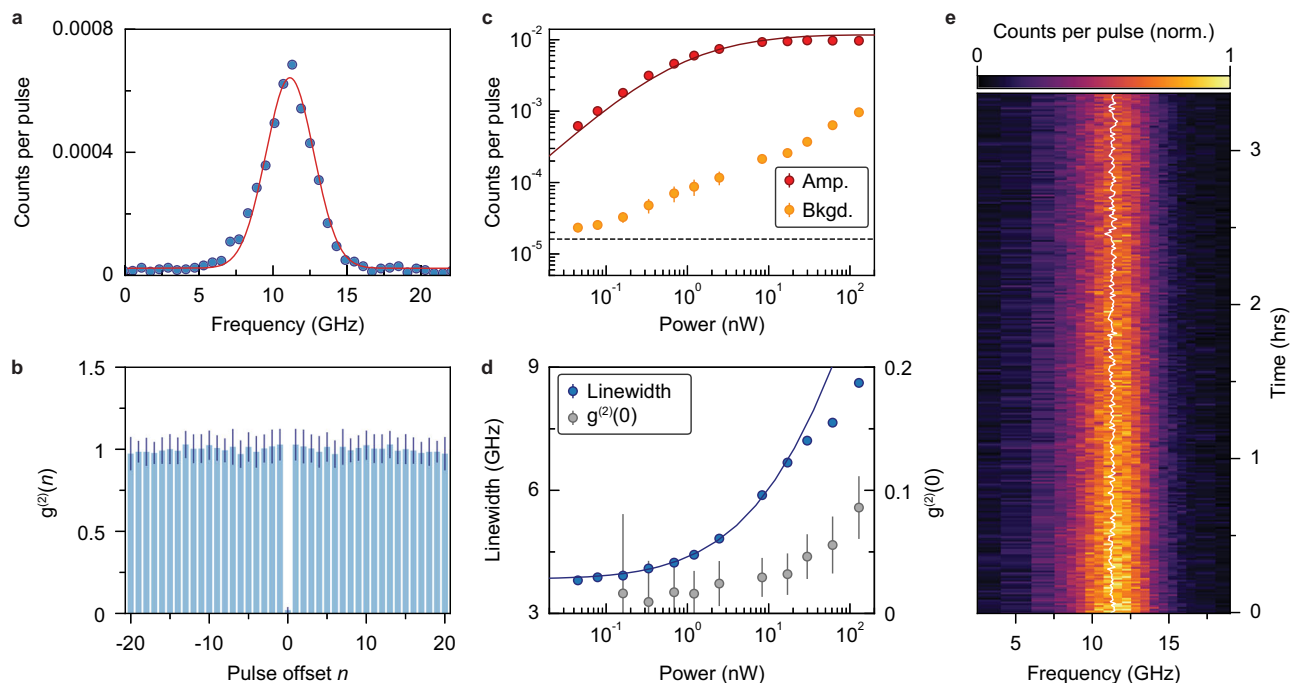


Fig. 3 | Cavity-coupled single T center characterizations. **a** PLE spectrum of the cavity-coupled single T center under an excitation power $P_{in} = 0.04$ nW. The red line shows the Gaussian fitting. **b** Second-order autocorrelation measurement for the same T center ($P_{in} = 2.47$ nW) shows a strong antibunching. All the photons detected after each excitation pulse are binned into a single-time bin. The horizontal axis shows the autocorrelation offset in units of the pulse repetition period (8 μ s). **c** Gaussian-fitted amplitude (Amp.) and background (Bkgd.) of single T-center PLE spectrum at different P_{in} . The background has the main contribution

from other weakly-coupled T centers beyond the SNSPD dark counts (3 Hz, black dashed line). The saturation behavior is well described by the numerical model (red line). **d** Spectrum linewidth of the single T center and the $g^{(2)}(0)$ at different P_{in} . The blue line shows the numerical calculation results. For results shown in panel (a–d), the cavity is tuned into resonance with the T center transition ($\Delta_{ac} = 0$). **e** Spectral diffusion of the single T center ($P_{in} = 8.31$ nW). White line shows the center of the spectrum at each iteration (with a duration of 42 seconds) of the experiment. In all plots, error bars denote $\pm 1\sigma$ statistical uncertainty.

observed for waveguide-coupled T centers (Supplementary Section 4). We note that this method only provides a lower bound of the Γ_{sd} due to the limited experiment repetition rate. We later turn to the numerical modeling to extract Γ_{sd} .

We apply a magnetic field (B) up to 300 mT along silicon [100] direction aiming to split the single T center line. We note that we have not been able to observe unambiguous Zeeman splitting using simultaneous two-tone laser sideband excitation, which is likely due to the limited splitting compared with the broad single T center linewidth. When using the single-tone laser excitation, the PLE amplitude decreases at increasing B field due to spin polarization³⁵. We model this behavior (Supplementary Section 5.4) to extract the difference of the excited- and ground-state g -factors $|\Delta_g| = 0.55 \pm 0.04$, which matches with one of the two predicted $|\Delta_g|$ values for T centers under a B field along the silicon [100] direction³⁵.

Purcell enhancement and numerical modeling

Lastly, we study the cavity-QED of the coupled system. When the cavity is tuned into resonance, the single T center's fluorescence lifetime is shortened to 136.4 ± 0.6 ns (Fig. 4a), which is 6.89 ± 0.03 times faster than the bulk lifetime of $1/\Gamma_0 = 940$ ns²³. Leveraging this enhanced decay, we extract an average ZPL photon outcoupling rate of 73.3 kHz at saturation for the cavity-coupled single T center. To confirm the enhancement originates from the cavity coupling, we measure the fluorescence decay rate Γ_{cav} at different cavity detunings (Δ_{ac}) (Fig. 4b), which can be described as $\Gamma_{cav}/\Gamma_0 = P_t/[1 + (2\Delta_{ac}/\bar{\kappa})^2] + \Gamma_\infty/\Gamma_0$, where $P_t = 5.88 \pm 0.04$ is the Purcell factor describing the fluorescence decay enhancement due to the cavity, $\Gamma_\infty = (1.03 \pm 0.02)\Gamma_0 \approx \Gamma_0$ is the asymptotic decay rate at large detunings, and $\bar{\kappa}/2\pi = 7.11 \pm 0.09$ GHz is the characteristic linewidth. To explain the deviation of $\bar{\kappa}$ from the cavity linewidth $\kappa/2\pi = 5.22$ GHz, we turn to numerical calculations by solving

the Lindblad master equation. Beyond the cavity and atomic loss channels, we also incorporate the pure dephasing and spectral diffusion processes (Supplementary Section 6.1). The dynamics of the coupled system can be described by the Jaynes-Cummings Hamiltonian of the form,

$$H/\hbar = \Delta_a \sigma_+ \sigma_- + \Delta_c a^\dagger a + g(\sigma_+ a + \sigma_- a^\dagger) + \frac{\Omega}{2}(\sigma_+ + \sigma_-), \quad (1)$$

which assumes rotating wave approximation in the rotating frame of the laser field (ω_L). Here $\Delta_a = \omega_a - \omega_L$ and $\Delta_c = \omega_c - \omega_L$ are, respectively, the detunings of the laser from the T center transition ω_a and the cavity resonance ω_c ; g is the coupling rate between the single T center and the cavity mode, and Ω is the optical Rabi frequency. The global fitting of the experimental data based on the numerical calculations given the known κ and Γ_0 (Supplementary Section 6.1), reveals the full cavity-QED parameter set $(g, \kappa, \Gamma_0) = 2\pi \times (42.4$ MHz, 5.22 GHz, 169.3 kHz), an excited-state dephasing rate $2\Gamma_d = 2\pi \times 1.29$ GHz, and a spectral diffusion $\Gamma_{sd} = 2\pi \times 1.69$ GHz. The characteristic linewidth $\bar{\kappa}$ has contributions from the cavity linewidth κ as well as Γ_d and Γ_{sd} . The model can simultaneously capture the saturation (Fig. 3c), power-dependent linewidth (Fig. 3d), and detuning-dependent fluorescence decay (Fig. 4b) results. Beyond the dephasing and the spectral diffusion, the single T center linewidth also has a minor contribution from the thermal broadening, which we estimate as $\Gamma_{th} \sim 0.1$ GHz from the temperature-dependent linewidth measurements (Supplementary Section 5.5).

To find out the Purcell enhancement of the single T center ZPL (P_{ZPL}) and its quantum efficiency (η_{QE}), we express the total emission rate of a single T center in absence of a cavity as the summation of the emission rates into the ZPL and the phonon sideband (PSB), as well as

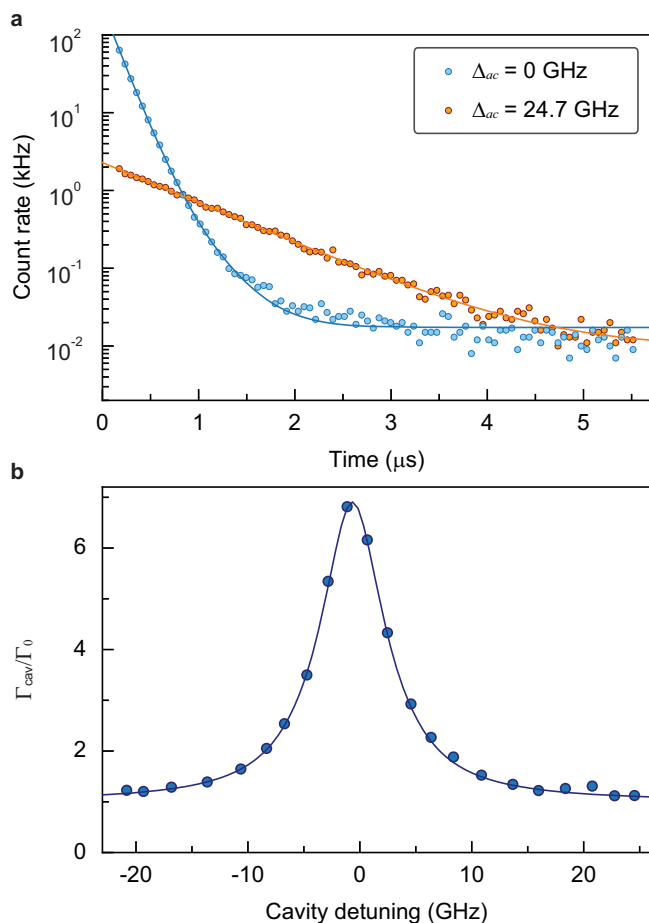


Fig. 4 | Cavity-enhanced fluorescence emission of the single T center. **a** Time-resolved fluorescence for the cavity-coupled single T center under saturation ($P_{\text{in}} = 17.01$ nW) with different cavity detunings. The exponential fitting (blue and orange lines) reveals decay lifetimes of 136.4 ± 0.6 ns and 835.2 ± 3.1 ns for $\Delta_{\text{ac}} = 0$ GHz and $\Delta_{\text{ac}} = 24.7$ GHz, respectively. **b** Decay rate enhancement at different cavity detunings with the laser fixed at the T center transition under an excitation power $P_{\text{in}} = 1.21$ nW. To gain better tuning accuracy, the cavity resonance is first retuned to $\Delta_{\text{ac}} = -20.8$ GHz, and subsequently blue-tuned. The blue line shows the numerical calculation results based on solving the Lindblad master equation.

nonradiative relaxation³⁷, $\Gamma_0 = \gamma_{\text{ZPL}} + \gamma_{\text{PSB}} + \gamma_{\text{nr}}$. The Debye-Waller (DW) factor and the quantum efficiency can then be defined as $\text{DW} = \gamma_{\text{ZPL}} / (\gamma_{\text{ZPL}} + \gamma_{\text{PSB}})$ and $\eta_{\text{QE}} = (\gamma_{\text{ZPL}} + \gamma_{\text{PSB}}) / \Gamma_0$, respectively. When the cavity is tuned into resonance with the T center ZPL, the cavity-enhanced decay rate is $\Gamma_{\text{cav}} = (P_{\text{ZPL}} + 1)\gamma_{\text{ZPL}} + \gamma_{\text{PSB}} + \gamma_{\text{nr}}$, where $P_{\text{ZPL}} = P_d / (\text{DW}\eta_{\text{QE}})$ is the Purcell factor describing the enhancement of the ZPL. We can thus put a lower bound on the $P_{\text{ZPL}} \geq P_d / \text{DW} = 25.6$, using the reported DW of 23%²³. For simplicity, we neglect the potential suppression of the γ_{PSB} due to the cavity³⁷. The ratio of the single T center ZPL emission coupled to the resonant cavity mode can be estimated as $\beta = P_{\text{ZPL}}\gamma_{\text{ZPL}} / [(P_{\text{ZPL}} + 1)\gamma_{\text{ZPL}} + \gamma_{\text{PSB}} + \gamma_{\text{nr}}] = P_t / (P_t + 1) = 85.5\%$. Due to sub-optimal positioning of the single T center inside the cavity and imperfect dipole alignment with the local cavity electrical field polarization, the P_{ZPL} extracted from measurements should be smaller than the simulated Purcell ($P_{\text{ZPL}} \leq P_{\text{ZPL}}^{\text{sim}}$). This enables us to put a lower bound on the quantum efficiency $\eta_{\text{QE}} \geq 23.4\%$ for the single T center (Supplementary Section 2.1).

Discussion

We now discuss pathways to improve the performance of the cavity-coupled single T center system. We note that the linewidth of the observed single T center is significantly larger than the

Purcell enhanced lifetime-limited linewidth ($2\pi \times 1.2$ MHz). One culprit is the fast dephasing process, which necessitates further investigation to reveal its origin. Significant reduction of Γ_{inh} down to 33 MHz has been demonstrated for ensemble T centers in enriched ^{28}Si ²³. In future work, SOI samples with an enriched silicon device layer can be prepared via molecular beam epitaxy³⁸ to minimize the dephasing. Furthermore, local electrodes can be fabricated on the SOI device layer for implementing electrical field control to minimize the spectral diffusion via in situ tuning³⁹ or depletion of the charge noises⁴⁰. Lastly, focused-ion-beam-based⁴¹ and masked⁴² ion implantation can be leveraged to increase the yield of T center generation at the cavity center.

In summary, we have demonstrated enhanced light-matter interaction for a single T center by integrating it with a silicon nanophotonic cavity. This work opens the door to utilize single T centers in silicon for quantum information processing and networking applications. With realistic improvements in the quality factor of the optical cavity ($Q = 5 \times 10^5$) and narrower linewidth in an enriched sample ($\Gamma = 10$ MHz), a large atom-cavity cooperativity $C \geq 29$ can be expected, which can lead to applications for high-fidelity dispersive spin readout⁴³ and cavity-mediated spin-spin interactions⁴⁴. Moreover, the current approach can enable parallel control and readout of multiple T centers in the cavity via the frequency domain addressing technique⁴⁵. Finally, leveraging the mature silicon photonics technology, small-footprint and scalable T-center-spin-based silicon quantum photonic chips¹³ may be envisioned.

Note: While finalizing this manuscript, we became aware of a related publication on the detection of a single T center coupled to a cavity using above-band excitation⁴⁶.

Methods

Device nanofabrication

All of the nanophotonic devices are fabricated on SOI samples (WaferPro). The SOI has a 220 ± 10 nm float zone grown P-type device layer with resistivity $\geq 1000 \Omega \cdot \text{cm}$. The buried oxide has a customized thickness of $2.3 \mu\text{m}$ for maximizing the GC coupling efficiency, and the handling layer has a thickness of $725 \mu\text{m}$. We spin coat 400 nm electron beam (ebeam) resist ZEP520A (Zeon Specialty Materials Inc.) onto $9 \times 9 \text{ mm}^2$ SOI chips and bake at 170°C for 5 mins. The sample is exposed using an Elionix ELS-G100 ebeam writer with a dosage of $225 \mu\text{C}/\text{cm}^2$, and subsequently developed in o-xylene at room temperature for 90 seconds and rinsed in isopropanol for 20 seconds. The pattern is then defined on the resist layer, which acts as the etching mask. The sample etching is performed using an inductively coupled plasma (ICP) reactive ion etcher (Oxford Plasmalab System 100/ICP 180) with $\text{SF}_6/\text{C}_4\text{F}_8$ gases. The sample is kept at 0°C during the etching process. After etching, the sample goes through a series of processes including oxygen plasma descum, dicing (into $4.5 \times 4.5 \text{ mm}^2$), resist stripping, and piranha cleaning before being transferred into the cryostat for measurements.

T center generation via ion implantation

T centers shown in this work are generated via a uniform ion implantation method following a published procedure³⁵. We use an equal fluence for ^{12}C and ^1H during the ion implantation processes (II-VI Coherent Corp). We perform ^{12}C ion implantation at 7° direction, 35 keV energy, followed by rapid thermal annealing (RTA) at 1000°C for 20 s under an Ar background to repair lattice damage and substitute the implanted carbon²⁴. Next, a second round implantation of ^1H at 7° direction, 8 keV energy is performed. After the two implantation steps, we boil the sample for 1 h in DI water, followed by a second RTA process at 420°C for 3 min with a N_2 background.

Data availability

The data that support the findings of this study are openly available on the Harvard Dataverse at <https://doi.org/10.7910/DVN/XCS15A>.

References

1. Awschalom, D. D., Hanson, R., Wrachtrup, J. & Zhou, B. B. Quantum technologies with optically interfaced solid-state spins. *Nat. Photon.* **12**, 516–527 (2018).
2. Togan, E. et al. Quantum entanglement between an optical photon and a solid-state spin qubit. *Nature* **466**, 730–734 (2010).
3. Bernien, H. et al. Heralded entanglement between solid-state qubits separated by three metres. *Nature* **497**, 86–90 (2013).
4. Pfaff, W. et al. Unconditional quantum teleportation between distant solid-state quantum bits. *Science* **345**, 532–535 (2014).
5. Bhaskar, M. K. et al. Experimental demonstration of memory-enhanced quantum communication. *Nature* **580**, 60–64 (2020).
6. Li, Q., Davanço, M. & Srinivasan, K. Efficient and low-noise single-photon-level frequency conversion interfaces using silicon nanophotonics. *Nat. Photon.* **10**, 406–414 (2016).
7. Wolfowicz, G. et al. Vanadium spin qubits as telecom quantum emitters in silicon carbide. *Sci. Adv.* **6**, eaaz1192 (2020).
8. Zhou, Y. et al. Room temperature solid-state quantum emitters in the telecom range. *Sci. Adv.* **4**, eaar3580 (2018).
9. Dibos, A., Raha, M., Phenicie, C. & Thompson, J. D. Atomic source of single photons in the telecom band. *Phys. Rev. Lett.* **120**, 243601 (2018).
10. Ourari, S. et al. Indistinguishable telecom band photons from a single Er ion in the solid state. *Nature* **620**, 977–981 (2023).
11. Kim, J.-H. et al. Hybrid integration of solid-state quantum emitters on a silicon photonic chip. *Nano Lett.* **17**, 7394–7400 (2017).
12. Wan, N. H. et al. Large-scale integration of artificial atoms in hybrid photonic circuits. *Nature* **583**, 226–231 (2020).
13. Pelucchi, E. et al. The potential and global outlook of integrated photonics for quantum technologies. *Nat. Rev. Phys.* **4**, 194–208 (2022).
14. Steger, M. et al. Quantum information storage for over 180 s using donor spins in a ²⁸Si “semiconductor vacuum”. *Science* **336**, 1280–1283 (2012).
15. Yin, C. et al. Optical addressing of an individual erbium ion in silicon. *Nature* **497**, 91–94 (2013).
16. Gritsch, A., Weiss, L., Früh, J., Rinner, S. & Reiserer, A. Narrow optical transitions in erbium-implanted silicon waveguides. *Phys. Rev. X* **12**, 041009 (2022).
17. Berkman, I. R. et al. Millisecond electron spin coherence time for erbium ions in silicon. *arXiv* <https://doi.org/10.48550/arXiv.2307.10021> (2023).
18. Chartrand, C. et al. Highly enriched ²⁸Si reveals remarkable optical linewidths and fine structure for well-known damage centers. *Phys. Rev. B* **98**, 195201 (2018).
19. Beauvils, C. et al. Optical properties of an ensemble of G-centers in silicon. *Phys. Rev. B* **97**, 035303 (2018).
20. Redjem, W. et al. Single artificial atoms in silicon emitting at telecom wavelengths. *Nat. Electron.* **3**, 738–743 (2020).
21. Komza, L. et al. Indistinguishable photons from an artificial atom in silicon photonics. *arXiv* <https://doi.org/10.48550/arxiv.2211.09305> (2022).
22. Prabhu, M. et al. Individually addressable and spectrally programmable artificial atoms in silicon photonics. *Nat. Commun.* **14**, 2380 (2023).
23. Bergeron, L. et al. Silicon-integrated telecommunications photon-spin interface. *PRX Quantum* **1**, 020301 (2020).
24. Higginbottom, D. B. et al. Optical observation of single spins in silicon. *Nature* **607**, 266–270 (2022).
25. DeAbreu, A. et al. Waveguide-integrated silicon T centres. *Opt. Express* **31**, 15045–15057 (2023).
26. Tait, A. N. et al. Microring resonator-coupled photoluminescence from silicon W centers. *J. Phys. Photon.* **2**, 045001 (2020).
27. Baron, Y. et al. Detection of single W-centers in silicon. *ACS Photon.* **9**, 2337–2345 (2022).
28. Lee, C.-M. et al. High-efficiency single photon emission from a silicon T-center in a nanobeam. *ACS Photon.* **10**, 3844–3849 (2023).
29. Purcell, E. M. Spontaneous emission probabilities at radio frequencies. In *Confined Electrons and Photons: New Physics and Applications*, 839–839 (Springer, 1995).
30. Lefaucher, B. et al. Cavity-enhanced zero-phonon emission from an ensemble of G centers in a silicon-on-insulator microring. *Appl. Phys. Lett.* **122**, 061109 (2023).
31. Redjem, W. et al. All-silicon quantum light source by embedding an atomic emissive center in a nanophotonic cavity. *Nat. Commun.* **14**, 3321 (2023).
32. Saggio, V. et al. Cavity-enhanced single artificial atoms in silicon. *arXiv* <https://doi.org/10.48550/arXiv.2302.10230> (2023).
33. Chen, S. et al. Hybrid microwave-optical scanning probe for addressing solid-state spins in nanophotonic cavities. *Opt. Express* **29**, 4902–4911 (2021).
34. Liu, L., Pu, M., Yvind, K. & Hvam, J. M. High-efficiency, large-bandwidth silicon-on-insulator grating coupler based on a fully-etched photonic crystal structure. *Appl. Phys. Lett.* **96**, 051126 (2010).
35. MacQuarrie, E. et al. Generating T centres in photonic silicon-on-insulator material by ion implantation. *N. J. Phys.* **23**, 103008 (2021).
36. Meunier, M. et al. Telecom single-photon emitters in GaN operating at room temperature: embedment into bullseye antennas. *Nanophotonics* **12**, 1405–1419 (2023).
37. Johnson, S. et al. Tunable cavity coupling of the zero phonon line of a nitrogen-vacancy defect in diamond. *N. J. Phys.* **17**, 122003 (2015).
38. Liu, Y. et al. ²⁸Silicon-on-insulator for optically interfaced quantum emitters. *J. Cryst. Growth* **593**, 126733 (2022).
39. Acosta, V. et al. Dynamic stabilization of the optical resonances of single nitrogen-vacancy centers in diamond. *Phys. Rev. Lett.* **108**, 206401 (2012).
40. Anderson, C. P. et al. Electrical and optical control of single spins integrated in scalable semiconductor devices. *Science* **366**, 1225–1230 (2019).
41. Schröder, T. et al. Scalable focused ion beam creation of nearly lifetime-limited single quantum emitters in diamond nanostructures. *Nat. Commun.* **8**, 15376 (2017).
42. Toyli, D. M., Weis, C. D., Fuchs, G. D., Schenkel, T. & Awschalom, D. D. Chip-scale nanofabrication of single spins and spin arrays in diamond. *Nano Lett.* **10**, 3168–3172 (2010).
43. Nguyen, C. et al. An integrated nanophotonic quantum register based on silicon-vacancy spins in diamond. *Phys. Rev. B* **100**, 165428 (2019).
44. Evans, R. E. et al. Photon-mediated interactions between quantum emitters in a diamond nanocavity. *Science* **362**, 662–665 (2018).
45. Chen, S., Raha, M., Phenicie, C. M., Ourari, S. & Thompson, J. D. Parallel single-shot measurement and coherent control of solid-state spins below the diffraction limit. *Science* **370**, 592–595 (2020).
46. Islam, F. et al. Cavity-enhanced emission from a silicon T center. *Nano. Lett.* **24**, 319–325 (2024).

Acknowledgements

We gratefully acknowledge Han Pu, Alexey Belyanin, and Tanguy Terlier for helpful discussions, and John Bartholomew for feedback on a manuscript draft. Support for this research was provided by the National Science Foundation (NSF, CAREER Award No. 2238298), the Robert A. Welch Foundation (Grant No. C-2134) and the Rice Faculty Initiative

Fund. We acknowledge the use of cleanroom facilities supported by the Shared Equipment Authority at Rice University.

Author contributions

A.J., U.F., Y.W. and S.C. contributed to the design and execution of the experiment. Y.W. and S.C. performed numerical modeling of the cavity-QED. A.J., U.F., Y.W. and S.C. analyzed the data and wrote the manuscript. S.C. supervised the whole project.

Competing interests

The authors declare no competing interests.

Additional information

Supplementary information The online version contains supplementary material available at

<https://doi.org/10.1038/s41467-024-46643-8>.

Correspondence and requests for materials should be addressed to Songtao Chen.

Peer review information *Nature Communications* thanks Weibo Gao, and the other, anonymous, reviewer(s) for their contribution to the peer review of this work. A peer review file is available.

Reprints and permissions information is available at <http://www.nature.com/reprints>

Publisher's note Springer Nature remains neutral with regard to jurisdictional claims in published maps and institutional affiliations.

Open Access This article is licensed under a Creative Commons Attribution 4.0 International License, which permits use, sharing, adaptation, distribution and reproduction in any medium or format, as long as you give appropriate credit to the original author(s) and the source, provide a link to the Creative Commons licence, and indicate if changes were made. The images or other third party material in this article are included in the article's Creative Commons licence, unless indicated otherwise in a credit line to the material. If material is not included in the article's Creative Commons licence and your intended use is not permitted by statutory regulation or exceeds the permitted use, you will need to obtain permission directly from the copyright holder. To view a copy of this licence, visit <http://creativecommons.org/licenses/by/4.0/>.

© The Author(s) 2024